

Scattering of elastic waves in geometrically anisotropic random media and its implication to sounding of heterogeneity in the Earth's deep interior

Tae-Kyung Hong* and Ru-Shan Wu

Earth Sciences Department/IGPP, University of California Santa Cruz, 1156 High Street, Santa Cruz, CA 95064, USA

Accepted 2005 July 25. Received 2005 May 27; in original form 2004 June 22

SUMMARY

The scattering features of elastic waves in media with geometrically anisotropic heterogeneities are investigated in terms of scattering attenuation, coda level and scattering directivity. The theoretical variation of scattering attenuation with normalized wavenumber (ka) is formulated using the multiple forward scattering and single backscattering approximation. Estimates obtained from numerical simulations agree with the theoretical predictions well. The level of scattering is influenced by the anisotropy (aspect ratio, direction) and the wave incidence direction. The scattering level is not sensitive to the scale variation in the wave incidence direction, but is highly sensitive to the scale variation in the tangential direction. Forward scattering is dominant when waves are incident along the major direction of geometrically anisotropic heterogeneity, and backward scattering is dominant when the waves are incident in the minor direction. The scattered energy is not distributed isotropically in media with anisotropic heterogeneity, and the level of early coda varies with the wave incidence angle. The late coda is composed of multiscattered and multipathing waves, and displays a stochastically stable energy level. The incidence angle of waves is a key parameter in the early coda variation, and an approach with classified seismic data for incidence angle is desired in the study of anisotropic heterogeneity in Earth's deep interior from seismic coda and precursor.

Key words: attenuation, elastic waves, geometrical anisotropy, minimum scattering angle, numerical modelling, scattering, theory, wavelet-based method, wavelets.

1 INTRODUCTION

Rigorous efforts have been made to investigate heterogeneities in the Earth's deep interior (e.g. Hedlin *et al.* 1997; Kennett *et al.* 1998). The sounding of the Earth's deep interior using traveltimes information or waveform inversion is useful with low-frequency seismic waves, which reflect large- (or global-) scale variation. On the other hand, probing with scattered waves, which appear in a form of precursors or coda waves in seismograms, allows us to investigate small-scale heterogeneity in the Earth. The inversion of scattered waves has been based on a stochastic approach assuming uniformly distributed isotropic heterogeneity (e.g. Hedlin *et al.* 1997; Lee *et al.* 2003).

The stochastic representation approach, however, suffers from non-uniqueness as usual inversion techniques do. In an analysis of seismic precursor of PKP, Hedlin *et al.* (1997) and Cormier (1999) presented a small-scale heterogeneity distribution model

of the lower mantle, where isotropic random heterogeneities with scale of 8 km and velocity perturbation of 1 per cent are distributed uniformly up to 1000 km above the core–mantle boundary (CMB). Another heterogeneity model compatible to the observed scattering strength is a model with strongly perturbed narrow zones at the lowermost mantle (Hedlin *et al.* 1997). Later, Margerin & Nolet (2003) confirmed the former model by an envelope inversion technique based on a radiative transport theory, which is formulated with an idea that the total transported scattered energy can be computed by radiated energy intensity including multiscattered energy.

The stochastic representation based on isotropic random heterogeneities, thus, provides us a fairly good insight on the physical and chemical environment in the Earth's deep interior despite the non-unique determination (e.g. Vidale & Hedlin 1998; Vidale & Earle 2000). However, geometrically anisotropic heterogeneities in the Earth are reported from seismic tomography studies (e.g. Kennett *et al.* 1998; Romanowicz 2003). Thus, it may be more reasonable to consider anisometric heterogeneity for the description of heterogeneity in the Earth. However, the scattering features by anisometric heterogeneities are known very little.

*Now at: Lamont-Doherty Earth Observatory of Columbia University, Palisades, NY 10964, USA. E-mail: tkhong@ldeo.columbia.edu

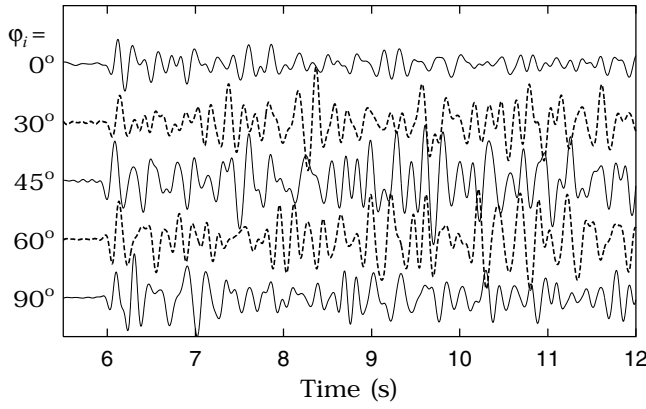


Figure 1. Synthetic P -wave record sections from geometrical anisotropic random media at various incidence angles ($\varphi_i = 0, 30, 45, 60, 90^\circ$). The anisometric heterogeneity is horizontally elongated, and the scales are 4010 m in the horizontal direction and 501 m in the vertical direction. The propagation distance is 49.1 km. The other physical properties of the medium are described in Section 5. The waveforms in both primary and coda change drastically with the incidence angle.

The scattering attenuation in anisometric random medium has been investigated in a limited view previously, for instance, paraxial wave incidence on anisometric heterogeneous medium (Wagner & Langston 1992; Roth & Korn 1993). Recently, traveltimes variation (Samuelides & Mukerji 1998; Iooss *et al.* 2000; Kravtsov *et al.* 2003) and amplitude fluctuation (Müller & Shapiro 2003) in anisometric random media were investigated in terms of incidence angle. However, the influence of the incidence angle on scattering attenuation remains still unclear, and the way to investigate anisometric heterogeneities has been rarely discussed.

In scattering by anisometric heterogeneity, the incidence angle to the heterogeneity looks an important factor. Because apparent scale of heterogeneity varies with the incidence direction. In Fig. 1, synthetic record sections from anisometric random media are presented. The waveforms in both primary and coda change drastically with the incidence angle. Thus, the investigation of scattering features for change of incidence angle will help us to understand more clearly the physical composition in the Earth's interior. In particular, the core phases, PKP , display a specific incidence angle to the CMB with epicentral distance; for instance, PKP_{df} ($PKIKP$) shows a nearly vertical incidence to the CMB at distances around 180° , and the incidence angle of the PKP_{bc} branch varies from about 30° to 60° at distances around 140° .

In this study, we mainly focus on the investigation of scattering attenuation variation, coda and scattered energy transmission in anisometric random media. For this purpose, we formulate a theoretical scattering attenuation expression for anisometric media. The theoretical expression is compared with the estimates from numerical simulations. Various sets of physical parameters are considered for models, and the influence of each parameter on scattering is investigated. In particular, the influence of incidence angle on the scattering energy distribution and coda level is discussed. Also, the difference in scattering between anisometric and isotropic random media is examined. Finally, we discuss the way to estimate correctly the physical property of anisometric heterogeneity in the Earth from observed seismic data.

2 THEORETICAL EXPRESSION OF SCATTERING ATTENUATION IN ANISOMETRIC RANDOM MEDIA

Theoretical scattering attenuation expression for anisometric random media can be formulated by expanding the approach for isotropic random media (Hong & Kennett 2003a; Hong 2004). Note that Wu & Aki (1985b) derived a general formulation of scattering coefficients, which can be applied to both isotropic and anisometric random media.

Here we consider the scattering of 2-D elastic waves. The 2-D elastic wave equations are given by

$$\rho_0 \frac{\partial^2 u_x^0}{\partial t^2} = \frac{\partial \sigma_{xx}^0}{\partial x} + \frac{\partial \sigma_{xz}^0}{\partial z}, \quad \rho_0 \frac{\partial^2 u_z^0}{\partial t^2} = \frac{\partial \sigma_{zx}^0}{\partial x} + \frac{\partial \sigma_{zz}^0}{\partial z}, \quad (1)$$

where

$$\sigma_{xx}^0 = (\lambda_0 + 2\mu_0) \frac{\partial u_x^0}{\partial x} + \lambda_0 \frac{\partial u_z^0}{\partial z},$$

$$\sigma_{zz}^0 = \lambda_0 \frac{\partial u_x^0}{\partial x} + (\lambda_0 + 2\mu_0) \frac{\partial u_z^0}{\partial z}, \quad (2)$$

$$\sigma_{xz}^0 = \mu_0 \left(\frac{\partial u_x^0}{\partial z} + \frac{\partial u_z^0}{\partial x} \right) \quad (3)$$

and λ_0 and μ_0 are the Lamé coefficients, and ρ_0 is the density in the background medium.

The perturbations in physical parameters ($\rho = \rho_0 + \delta\rho$, $\lambda = \lambda_0 + \delta\lambda$, $\mu = \mu_0 + \delta\mu$) cause wave scattering, and can be treated as equivalent body forces (f_x^s , f_z^s) for the scattered field:

$$\rho \frac{\partial^2 u_x^0}{\partial t^2} - \frac{\partial \sigma_{xx}^0}{\partial x} - \frac{\partial \sigma_{xz}^0}{\partial z} = f_x^s, \quad \rho \frac{\partial^2 u_z^0}{\partial t^2} - \frac{\partial \sigma_{zx}^0}{\partial x} - \frac{\partial \sigma_{zz}^0}{\partial z} = f_z^s. \quad (4)$$

For vertically incident P waves ($u_x^0 = 0$, $u_z^0 = \exp[i(k_\alpha z - \omega t)]$), eq. (4) can be written by (Hong & Kennett 2003a)

$$f_x^s = -ik_\alpha \frac{\partial(\delta\lambda)}{\partial x} u_z^0,$$

$$f_z^s = - \left\{ k_\alpha^2 (\alpha_0^2 \delta\rho - \delta\lambda - 2\delta\mu) + ik_\alpha \frac{\partial(\delta\lambda + 2\delta\mu)}{\partial z} \right\} u_z^0. \quad (5)$$

Here, the variations of physical parameters in the Earth are strongly correlated to each other (Birch 1961; Shiomi *et al.* 1997; Romanowicz 2001), so the S -wave velocity perturbation and the density perturbation can be expressed in terms of the P -wave velocity perturbation (ξ):

$$\xi(x, z) = \frac{\partial\alpha}{\alpha_0} = \frac{1}{K_\beta} \frac{\delta\beta}{\beta_0} = \frac{1}{K_\rho} \frac{\delta\rho}{\rho_0}, \quad (6)$$

where α_0 is the P -wave velocity in the background medium, β_0 the S -wave velocity, and ρ_0 the density. K_β and K_ρ are constants determining the relative strengths of S -velocity perturbation and density perturbation to the P -velocity perturbation.

Using the relationship in (6), the body forces in (5) can be expressed in terms of ξ :

$$f_x^s = -ik_\alpha \alpha_0^2 \rho_0 C_1 \frac{\partial\xi}{\partial x} \exp[i(k_\alpha z - \omega t)],$$

$$f_z^s = \left(2k_\alpha^2 \alpha_0^2 \rho_0 \xi - ik_\alpha \alpha_0^2 \rho_0 C_2 \frac{\partial\xi}{\partial z} \right) \exp[i(k_\alpha z - \omega t)], \quad (7)$$

where C_1 and C_2 are

$$C_1 = (2 + K_\rho) - \frac{2}{\gamma^2} (2K_\beta + K_\rho), \quad C_2 = 2K_\beta + K_\rho \quad (8)$$

and $\gamma = \alpha_0/\beta_0$. The remaining derivation procedure follows the procedure in previous studies. A summarized derivation procedure of scattering attenuation is presented in Appendix A.

Finally, the theoretical scattering attenuation expression (Q^{-1}/ϵ^2), based on the multiple forward scattering and single backscattering approximation, is given by

$$\frac{Q_s^{-1}}{\epsilon^2} = \frac{k_\alpha^2 W_r}{(4\pi)^2} \int_{\theta_{\min}}^{2\pi-\theta_{\min}} \mathcal{P}(\mathbf{k}_r^*) d\theta + \frac{k_\alpha^2 \gamma^2 W_t}{(4\pi)^2} \int_{\theta_{\min}+\Delta\phi}^{2\pi-\theta_{\min}-\Delta\phi} \mathcal{P}(\mathbf{k}_t^*) d\theta, \quad (9)$$

where θ_{\min} is the minimum scattering angle, ϵ is the standard deviation of perturbation, \mathcal{P} is the power spectral density function, and $\Delta\phi$ is given by

$$\Delta\phi = \phi_P - \phi_S, \quad \phi_P = \frac{\pi - \theta_{\min}}{2}, \quad \phi_S = \sin^{-1} \left(\frac{\sin \phi_P}{\gamma} \right). \quad (10)$$

The wavenumber vector \mathbf{k}_j^* ($j = r, t$) is given by

$$\mathbf{k}_r^* = k_\alpha(1 - \cos\theta, -\sin\theta), \quad \mathbf{k}_t^* = k_\alpha(1 - \gamma \cos\theta, -\gamma \sin\theta), \quad (11)$$

and the coefficient W_j is

$$W_r = (64 + 7C_1^2 - 64C_2 + 28C_2^2)/32, \\ W_t = (64 - 64C_2 + 16C_2^2 + \gamma^2 C_1^2 + 4\gamma^2 C_2^2)/32. \quad (12)$$

Here, the coefficient W_j reflects the average coefficient strength for every scattering angle. The eq. (9) is the general scattering attenuation solution for anisometric random medium, and can be applied directly if the PSDF is known. The PSDF for paraxial incidence system can be formulated easily, but the PSDF for inclined incidence system needs to be formulated with consideration of incidence angle. The discussion is expanded in Section 4.

3 ANISOMETRIC RANDOM MEDIA

We follow the notation and the terminology used in the geostatistics (Deutsch & Journel 1998) for description of geometrically anisotropic model. The direction of the largest correlation distance is called the major direction, and the tangential direction, with the smallest correlation distance, is referred as the minor direction. The heterogeneity scales in the major and minor directions are used for the construction of anisometric structure.

We first consider paraxial systems where the major direction is along either of the coordinate axes. The anisometric random heterogeneity can be modelled by extending the isotropic heterogeneity expression. The 2-D exponential autocorrelation function (ACF, $N(\mathbf{x})$) of anisometric random heterogeneity and its power spectral density function (PSDF, $\mathcal{P}(\mathbf{k})$) are given by (e.g. Iooss 1998)

$$N(x, z) = \exp \left[-\frac{r'}{a'} \right], \quad \mathcal{P}(k_x, k_z) = \frac{2\pi V_a}{\left\{ 1 + (k'a')^2 \right\}^{3/2}}, \quad (13)$$

where a_x and a_z are the correlation distances (scales) of stochastic random heterogeneity in x - and z -axis directions, and k_x and k_z are the wavenumbers along the axis directions. The r'/a' , $k'a'$, and V_a in (13) are given by

$$\frac{r'}{a'} = \sqrt{\frac{x^2}{a_x^2} + \frac{z^2}{a_z^2}}, \quad k'a' = \sqrt{k_x^2 a_x^2 + k_z^2 a_z^2}, \quad V_a = a_x a_z. \quad (14)$$

The ACF and PSDF of Gaussian random medium are

$$N(x, z) = \exp \left[-\left(\frac{r'}{a'} \right)^2 \right], \quad \mathcal{P}(k_x, k_z) = \pi V_a \exp \left[-\frac{(k'a')^2}{4} \right], \quad (15)$$

and the von Karman ACF and PSDF are

$$N(x, z) = \frac{1}{2^{\nu-1} \Gamma(\nu)} \left(\frac{r'}{a'} \right)^\nu K_\nu \left(\frac{r'}{a'} \right), \\ \mathcal{P}(k_x, k_z) = \frac{4\pi \nu V_a}{\left\{ 1 + (k'a')^2 \right\}^{\nu+1}}, \quad (16)$$

where ν is the Hurst number, Γ is the Gamma function, and K_ν is the modified Bessel function of order of ν . Here the exponential random media correspond to von Karman media with Hurst number of 0.5.

4 EXPANSION TO INCLINED ANISOMETRIC RANDOM MEDIA

In anisometric random media, the stochastic heterogeneity scales in the incident and tangential directions change with the wave incidence angle. Thus, it is expected that the scattering strength changes with the incidence angle. This effect is observed in a form of azimuthal anisotropy in field data analysis. As the wave front approaching to the deep Earth is nearly planar, the incident waves are well defined with the incidence angle and the geometry of the anisometric system can be represented with the relative incidence angle for the anisometric heterogeneity.

For convenience in numerical simulation and analysis, the incidence angle is considered in the system by rotating the random medium instead of considering inclined wave incidence (see, Fig. 2a). The implementation of rotated anisometric medium provides several advantages over the consideration of inclined wave incidence. With application of periodic boundary condition at the left and right artificial boundaries of medium, we can imitate a horizontally unbounded random medium. Also, the scattered energy exchanged across the artificial boundaries can be considered correctly. Note that the incidence angle considered in this study is the relative angle between the wave incidence direction and the minor direction of heterogeneity. Thus, the results can be extended straightforwardly to field observation by considering the relative incidence angle.

We have presented the theoretical scattering attenuation expression for paraxial system in (9), where waves are incident along the major or minor direction. The scattering attenuation in a random medium is the stochastic energy loss by scattering on heterogeneities. The individual ray is interfered by perturbation along the ray path, and the scattering of incident waves is dominantly influenced by the apparent scales of heterogeneity in the incident and the tangential direction. Thus, the heterogeneity in inclined incidence system can be represented with stochastic scales in the incident and tangential directions.

The stochastic scales of inclined heterogeneity can be estimated through an angular rotation of the coordinate system (e.g. Samuelides & Mukerji 1998; Iooss *et al.* 2000):

$$\frac{1}{a_h} = \sqrt{\frac{\cos^2 \varphi_i}{a_x^2} + \frac{\sin^2 \varphi_i}{a_z^2}}, \quad \frac{1}{a_v} = \sqrt{\frac{\sin^2 \varphi_i}{a_x^2} + \frac{\cos^2 \varphi_i}{a_z^2}}, \quad (17)$$

where φ_i is the relative incidence angle and a_v is the stochastic scale in the wave incidence direction and a_h is the scale in the tangential direction. The theoretical variation of scattering attenuation

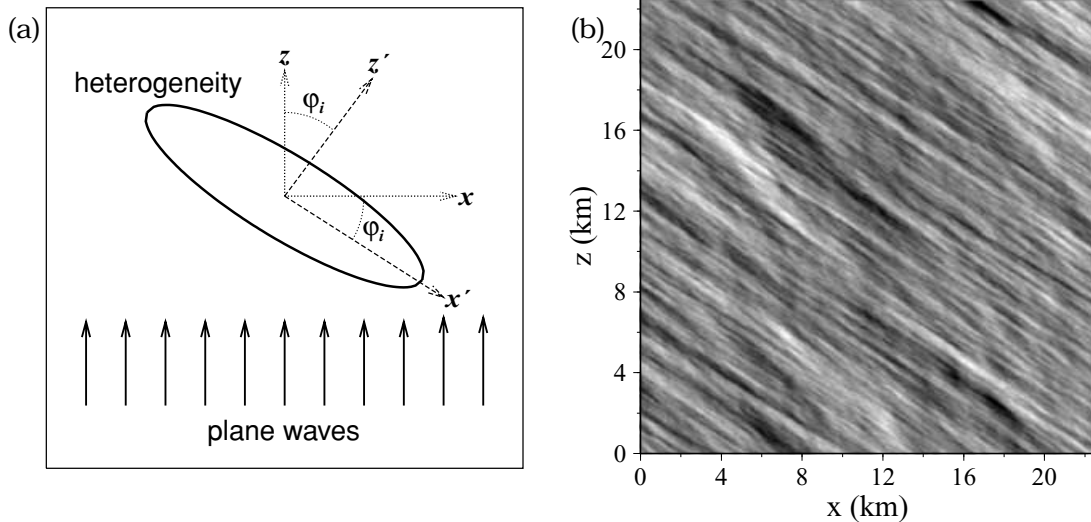


Figure 2. (a) The relative incidence angle (φ_i) is defined as the angle between the incidence direction (z) and the minimum direction of anisotropy (z'). x' -axis direction corresponds to the maximum direction of anisotropy, and x -axis direction is orthogonal to the incidence direction. (b) The geometrical anisotropic random medium with $a_x = 4010$ m, $a_z = 501$ m and $\varphi_i = 30^\circ$.

in inclined system can be estimated using the stochastic scales of heterogeneity, that is, a_h and a_v instead of a_x and a_z are applied to the computation of the spectral density functions (PSDF) in (13), (15) and (16). The theoretical scattering attenuation expression is validated by comparing to numerical results in Section 6.

5 NUMERICAL MODELLING

We consider a plausible set of physical properties at the upper mantle from the Earth model by Kennett *et al.* (1995). We set P -wave velocity to be 8.325 km s^{-1} , S -wave velocity 4.5 km s^{-1} , and the density 3.4 g cm^{-3} . The size of medium is $45 \times 90 \text{ km}$ and the domain is represented by 256×512 grid points. The top and bottom artificial boundaries are treated with absorbing boundary condition, and the artificial boundaries on both sides are considered to have periodic boundary condition that imitates horizontally unbounded media.

Plane P waves are incident vertically, and the source time function is the Ricker wavelet with dominant frequency of 4.5 Hz . 12 receiver arrays are deployed perpendicularly to the incidence direction at every 5.45 km from the source position along the incidence direction. Each receiver array consists of 256 receivers and the interval between adjacent receivers in a receiver array is 175.8 m . The propagation distances to the shortest and the longest receiver arrays are 5.45 and 65.39 km .

We consider the exponential anisometric random model (13). The random models are constructed in the wavenumber domain by assigning random phases to a spectral density function at each grid point (Hong & Kennett 2003a). The spectral random variation is converted to spatial random variation by Fourier transform. The inclined anisometric random media are designed by rotating a reference random model (see, Fig. 2b). We consider 5 per cent perturbation in P -wave velocity. The shear velocity perturbation is set to be twice the P velocity perturbation (i.e. $K_\beta = 2$), which is plausible in the mantle (see, Robertson & Woodhouse 1996; Romanowicz 2001). The density perturbation is much less resolvable from seismic data (Kennett 1998; Romanowicz 2001). Considering the general relationship between velocity and density in the Earth (Birch 1961; Sato

& Fehler 1998), we apply 4 per cent perturbation in the density (i.e. $K_\rho = 0.8$).

We consider the vertical scale of anisometric heterogeneity as the minor scale, and the horizontal scale as the major scale. We set the horizontal scale to vary in the order of 2 from 501 m through 1003 m and 2005 m to 4010 m , and the vertical scale (a_z) to be constant by 501 m . The apparent stochastic scales in inclined incidence system vary with the relative incidence angle (φ_i). When φ_i is 90° , the stochastic scale in the incidence direction (a_v) is equal to a_x . We consider five relative incidence angles (φ_i) of $0, 30, 45, 60$ and 90° in the modelling.

A wavelet-based method (Hong & Kennett 2002a,b, 2003b, 2004) is used for modelling of wave propagation in these random media. The wavelet-based method is based on the full wave equation, and the spatial differentiations (∂_x, ∂_z) in the wave equation are applied in the wavelet space using an operator projection technique. The spatial differentiation in wavelet space allows us to have accurate responses of both high- and low-frequency variation in medium. Hong & Kennett (2003a) pointed out that artificial attenuation can be included in numerical simulation in random media due to frequent variation in physical properties when a low order of numerical modelling technique is applied. Also, the wavelet-based method is numerically stable even in highly perturbed media, and thus suitable for modelling in random media.

6 SCATTERING ATTENUATION

Scattered waves are generated when waves encounter heterogeneities. In isotropic random media, the radiation pattern of incident waves controls the scattering energy distribution around a heterogeneity (Wu & Aki 1985a). In anisometric random media, the relative incidence angle plays an additional important role in the scattered energy distribution. Thus, the scattering feature in anisometric random medium can be identified with the relative incidence angle and the aspect ratio between the major and minor scales.

Fig. 3 displays synthetic time responses from anisometric random media with a_x of 4010 m and a_z of 501 m for various relative incidence angles ($\varphi_i = 0, 30, 45, 60, 90^\circ$). We present also the time responses from isotropic random medium ($a_x = a_z = 4010 \text{ m}$) for

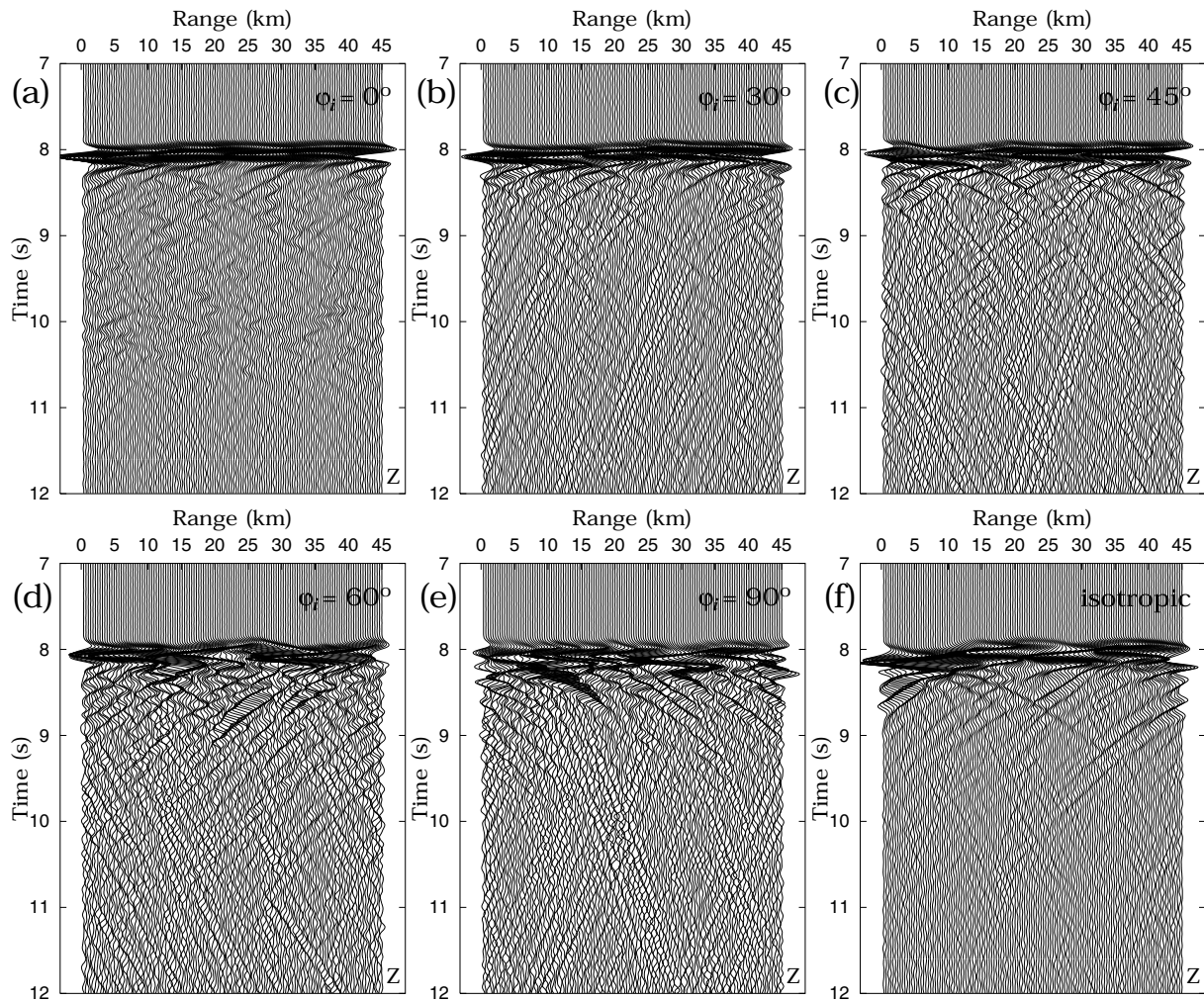


Figure 3. Time responses at media with $a_x = 4010$ m and $a_z = 501$ m for various incidence angles; (a) $\varphi_i = 0^\circ$, (b) 30° , (c) 45° , (d) 60° and (e) 90° . (f) Time responses at isotropic random media ($a_x = a_z = 4010$ m) are presented for comparison. Scattered wavefields of $\varphi_i = 0^\circ$ looks weaker than those of the isotropy case even though average scale of heterogeneity is larger in the isotropy case. The scattered wavefield of the isotropy case is composed of strong diffracted waves, which are observed weak in anisotropic media.

comparison. The phase and amplitude fluctuations and the scattering strength vary with the relative incidence angle (φ_i).

The phase fluctuation of primary waves is significant in isotropic random media due to the diffraction and refraction effect (Müller & Shapiro 2003). The apparent geometrical anisotropy decreases with relative incidence angle until 45° , and then increases until 90° (see, Fig. 4). The phase fluctuation observed in anisometric random media generally varies with the apparent anisotropy rate. The phase fluctuation of $\varphi_i = 60^\circ$, however, appears to be stronger than that of $\varphi_i = 45^\circ$ where the heterogeneities are stochastically isotropic due to the increase of forward scattering with the relative incidence angle and anisotropic energy distribution. The discussion is extended in the following section.

We measure scattering attenuation from synthetic time records of various relative incidence angles ($\varphi_i = 0, 30, 45, 60, 90^\circ$). Theoretical scattering attenuations from (9) are compared with the numerical results. The scattering attenuation of time records is measured using the Q definition (Aki & Richards 1980):

$$Q^{-1}(\omega) = \frac{2\alpha_0}{\omega r} \ln \left[\frac{A_0(\omega)}{A_r(\omega)} \right], \quad (18)$$

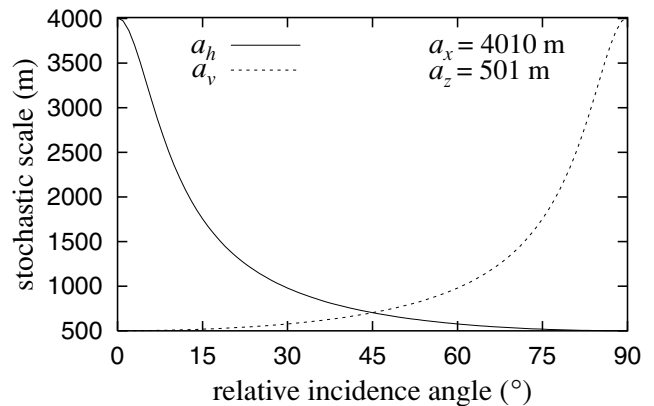


Figure 4. Stochastic-scale variation (a_h, a_v) with the relative incidence angle from equation (17) when a_x is 4010 m and a_z is 501 m. The horizontal stochastic scale (a_h) decreases fast with the relative incidence angle, and the decreasing rate is proportional to the aspect ratio (a_x/a_z).

where ω is angular frequency, r is the propagation distance, and A_0 and A_r are the spectral amplitudes at the origin and the receiver. The spectral amplitudes of primary waves are measured by stacking the amplitudes of tapered records (Hong & Kennett 2003a, 2004).

Scattering attenuation is over or underestimated at short distance, and stable scattering attenuation can be measured at a sufficiently large distance (Hong *et al.* 2005). The seismograms of the 12th receiver array, the furthest array from the source position, are used for the scattering attenuation measurement. In Fig. 5, we compare the

scattering attenuation in random media with theoretical prediction from eq. (9). The scattering attenuation variation in isotropic random media is also presented for comparison with those of anisometric media.

The theoretical scattering attenuation curves for inclined incidence systems in Fig. 5 are calculated using the stochastic scales of heterogeneity in the incident and tangential directions. In order to verify this approach, we construct paraxial anisometric system with use of the stochastic scales measured from inclined incidence

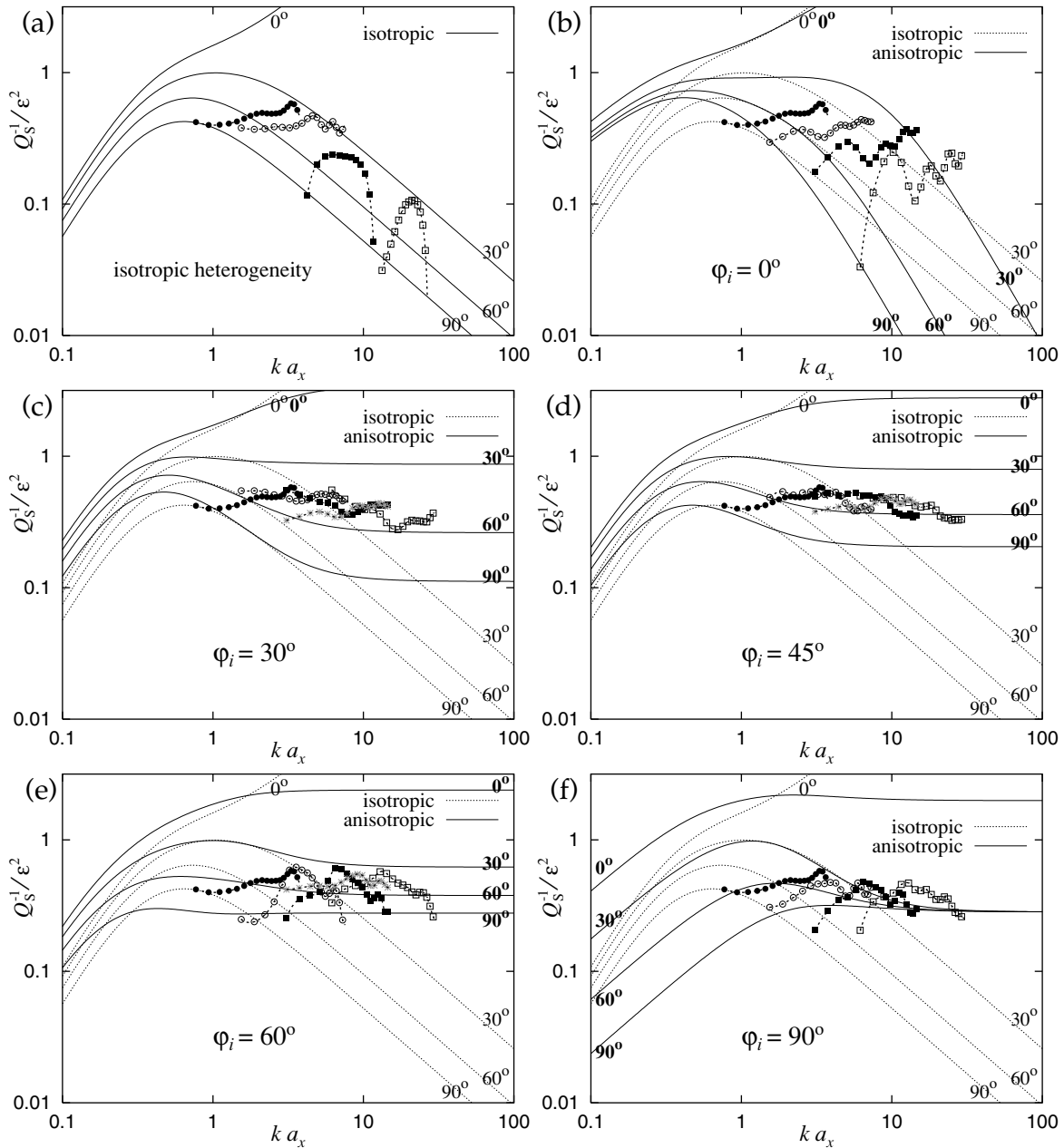


Figure 5. Scattering attenuation variations with normalized wavenumber (ka_x) in (a) isotropic random media and anisotropic random media of (b) $\varphi_i = 0^\circ$, (c) 30° , (d) 45° , (e) 60° and (f) 90° . The vertical heterogeneity scale (a_z) is set constant by 501 m ($k_d a_z = 1.7$, where k_d is the wavenumber of dominant frequency) in the anisotropic random media, but a_z is set equal to a_x in isotropy cases. Results are marked with filled circles ($a_x = 501$ m data set), open circles ($a_x = 1003$ m), closed squares ($a_x = 2005$ m) and open squares ($a_x = 4010$ m). For comparisons with scattering attenuations in inclined systems ($\varphi_i = 0, 30, 60^\circ$) for the case of $a_x = 2005$ m, those in corresponding paraxial incidence systems are presented in the figures with asterisks. The theoretical scattering attenuation curves from (9) are included for comparisons with numerical results. Also, the theoretical curves for isotropic random media are additionally included in the figures for anisotropy cases in order to understand the relative variation. The numerical results from media with 5 per cent of velocity perturbation are placed in a region between the theoretical curves with $\theta_{\min} = 30^\circ$ and 60° , and this result agrees with previous studies (e.g. Hong *et al.* 2004).

systems, and calculate time records. The scattering attenuations obtained from inclined incidence systems and their equivalent paraxial incidence systems are compared for cases of $a_x = 2005$ m and $a_z = 501$ m (see, Figs 5c–e). The scattering attenuations measured from the corresponding paraxial incidence systems are marked with asterisks in the figures. The scattering attenuations between the two systems are fairly close each other. This indicates that the scattering attenuation in anisometric random media is dependent mainly on the scales in the incident and tangential directions.

The measured scattering attenuations of all cases are placed in a zone between the theoretical curves with minimum scattering angle (θ_{\min}) of 30° and 60° . The minimum scattering angle is a stochastic angle span for correction of forward scattering energy that complements the primary wave (Hong 2004). As the perturbation strength in the medium increases, apparent coherent forward scattering is strengthened at large normalized wavenumber ($ka > 1$) (Hong *et al.* 2005). Thus, the minimum scattering angle appears to increase with perturbation strength at the large normalized wavenumber (Hong & Kennett 2003a; Hong *et al.* 2005).

We translate ka_x into ka_h using eq. (17), and present the scattering attenuation variation as function of ka_h for φ_i of $30^\circ, 45^\circ, 60^\circ$ (Fig. 6). The corresponding theoretical scattering attenuation curves are obtained using eqs (9) and (17). The systems of $\varphi_i = 0^\circ$ and 90° are the extreme cases where a_h corresponds to either a_x or a_z , that is, $a_h = a_x$ at $\varphi_i = 0^\circ$ and $a_h = a_z$ at $\varphi_i = 90^\circ$. Thus, the scattering

attenuation variations with ka_h at $\varphi_i = 0^\circ$ and 90° corresponds to Figs 5(b) and (e).

The trend of scattering attenuation variation with ka_h in anisometric random media is comparable to that of isotropic random media at the low ka_h regime ($ka_h < 3$). However, scattering attenuation in anisometric random media is much lower than that in isotropic random medium at high ka_h ($ka_h > 3$). That is, when a_h is large (i.e. aspect ratio a_x/a_z is large), scattering is weakened and diffraction and refraction is strengthened instead.

7 CODA AND ENERGY TRANSMISSION

7.1 General features

We investigate the scattered energy distribution with wave incidence direction at anisometric random media. In the previous section, it was shown that the energy lost by scattering in oblique incidence system can be calculated with an equivalent paraxial incidence system. The total energy in an elastic system is conserved, and the lost energy of primary waves by scattering propagates in a form of scattered waves. Also, when scattered wavefields are diffused, (i.e. in a static state of homogeneous energy distribution throughout the medium), it is expected that the coda waves of oblique incidence system and the equivalent paraxial incidence system display a same level of energy. Thus, comparison between the two systems

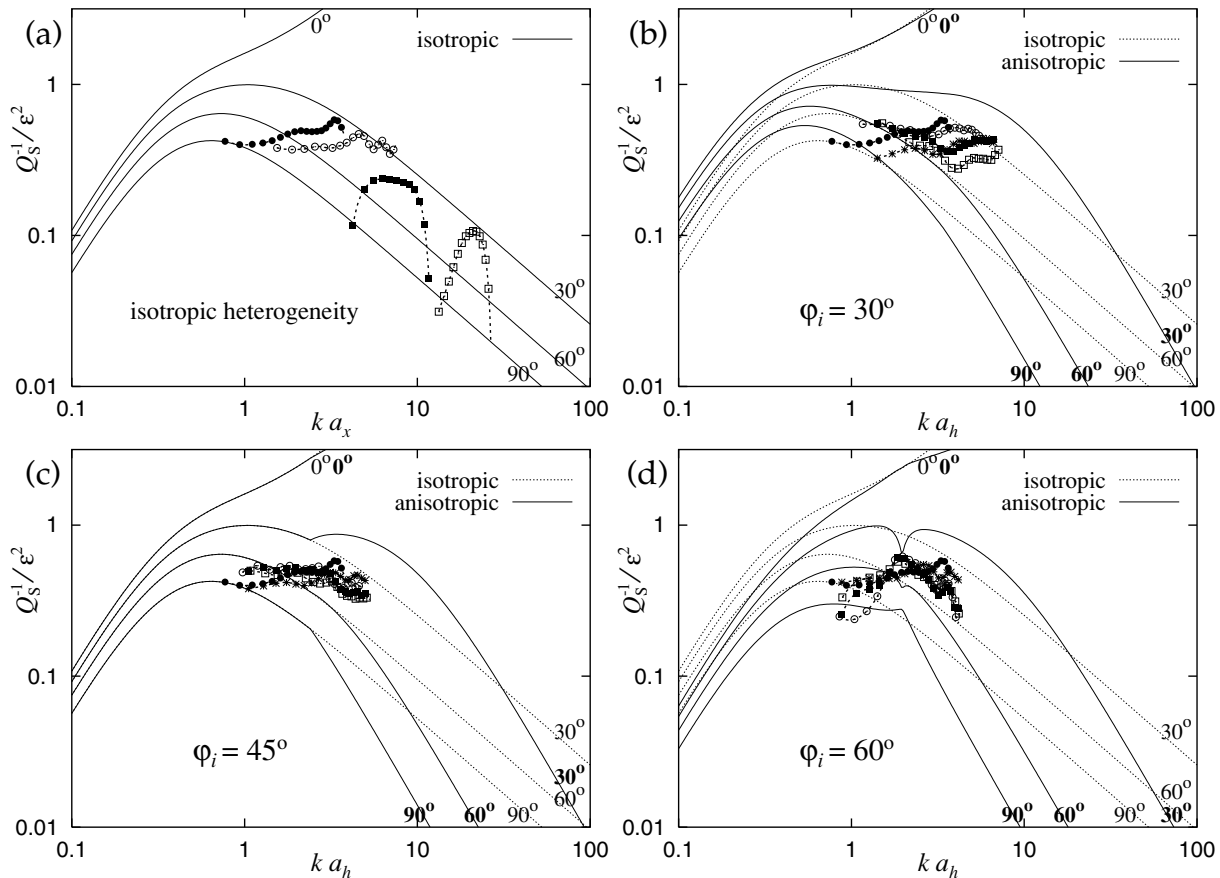


Figure 6. Scattering attenuation variations with ka_h in (a) isotropic random media and anisotropic random media of (b) $\varphi_i = 30^\circ$, (c) 45° and (d) 60° . The parameters and the symbols follow the notation in Fig. 5. The variation of scattering attenuation in isotropic random media which is presented in Fig. 5(a) for reference. Note that a_x is equal to a_h for isotropic random media. Scattering attenuations of anisometric is close to those of isotropic random media at low ka_h regime ($ka_h < 3$), and discrepancy is raised at large ka_h regime ($ka_h > 3$).

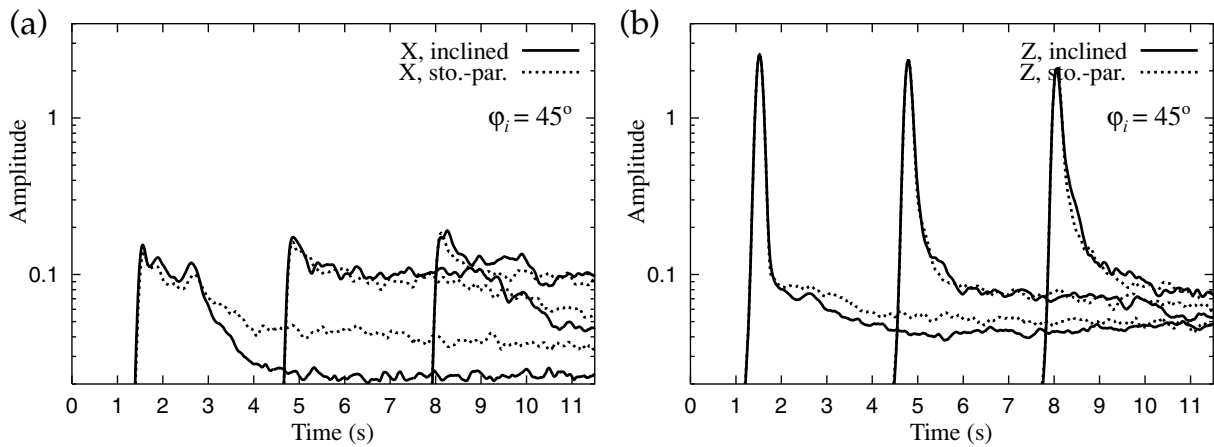


Figure 7. Comparisons of (a) x - and (b) z -component envelopes between an inclined system with $\phi_i = 45^\circ$ and its corresponding paraxial incidence system at propagation distances of 10.9, 38.1 and 65.4 km. The horizontal heterogeneity scale (a_x) of the inclined system is 2005 m, and the vertical scale (a_z) is 501 m. The rms envelopes are presented in Fig. 9(b).

will allow us to understand the temporal distribution of scattered energy.

The idea of measuring scattering power from local seismic coda at a time of homogeneous scattered-energy distribution has been applied widely in field data analyses after Aki & Chouet (1975) and Aki (1980). The scattering strength is expressed in either quality factor (e.g. Frankel *et al.* 1990; Yoshimoto *et al.* 1993) or scattering coefficient (Sato & Fehler 1998). As the heterogeneity distribution in the Earth is not uniform and the scale of heterogeneity varies with depth and lateral location, the quantification of teleseismic coda energy provides the stochastic average properties of all heterogeneities on propagation paths. The temporal variation of coda level is dependent mostly on the scattering radiation pattern and the spatial distribution of scatterers. Thus, the investigation of temporal coda level variation allows us to understand the scattered energy distribution in anisometric random media.

Fig. 7 shows the coda envelopes in x and z components for an anisometric random medium. The two coda envelopes are strongly correlated each other. Also, as the primary energy is partitioned during propagation in random media due to the phase fluctuation and diffraction on heterogeneity, a part of primary energy is recorded in

the tangential component (Hong & Kennett 2003a). Thus, we use the root-mean-square (rms) envelope of x - and z -component envelopes as the reference envelope (Fig. 8). The reference mean rms envelope is calculated by averaging all rms envelope of records (Fig. 8a). In this study, 256 synthetic records are used in the computation of the reference envelope. The standard deviation (σ) of each rms envelope from the reference envelope is far below the level of the mean envelope (8b). The normalized standard deviation, which is given by $\sigma/A_0(t)$ where $A_0(t)$ is the amplitude of the mean envelope at time t , is measured constant in coda by 0.37. In this study, we present the amplitudes of envelopes in a log scale to display the coda variation clearly. The amplitude range in the log scale is selected to display scientifically meaningful amplitudes (amplitudes larger than 0.005 times of primary-wave amplitude). An envelope in both a log scale and actual scale is shown in Fig. 8.

In Fig. 9, we compare the rms envelopes of oblique systems with those of their corresponding paraxial incidence systems at three distances ($r = 10.89, 38.14, 65.39$ km). The coda just after the primary waves (P wave in this study) of oblique system displays a higher amplitude than that of the paraxial incidence system. This energy accretion at the early coda in the inclined system is strengthened

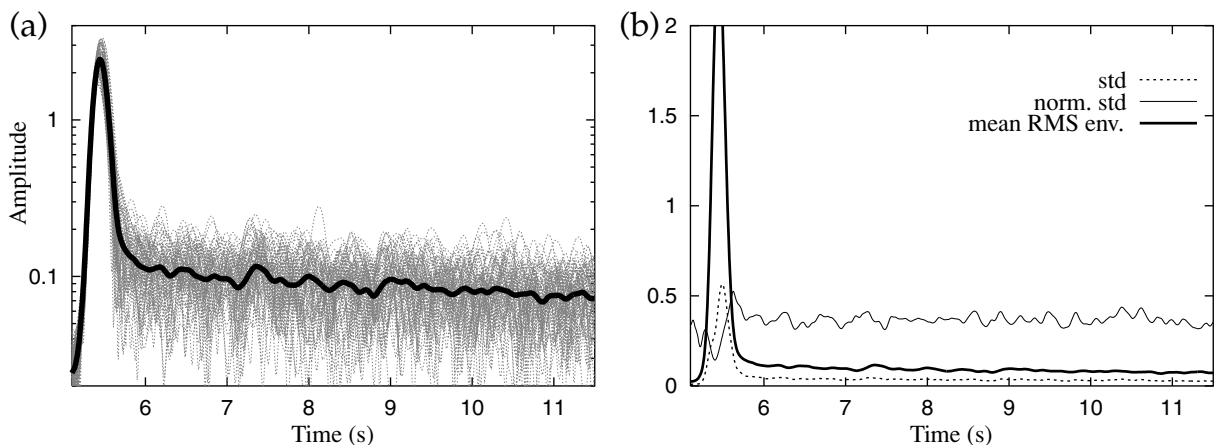


Figure 8. (a) Comparison between rms envelopes of all records and the reference envelope. (b) The standard deviation (σ) of the envelopes of records from the reference envelope and the normalized standard deviation, which is computed by dividing the standard deviation by the reference envelope (i.e. $\sigma/A_0(t)$). The standard deviation is far below the level of the reference envelope, and the normalized standard deviation is measured almost constant by around 0.37. The same reference envelope is plotted in a log scale in (a) and in actual scale in (b).

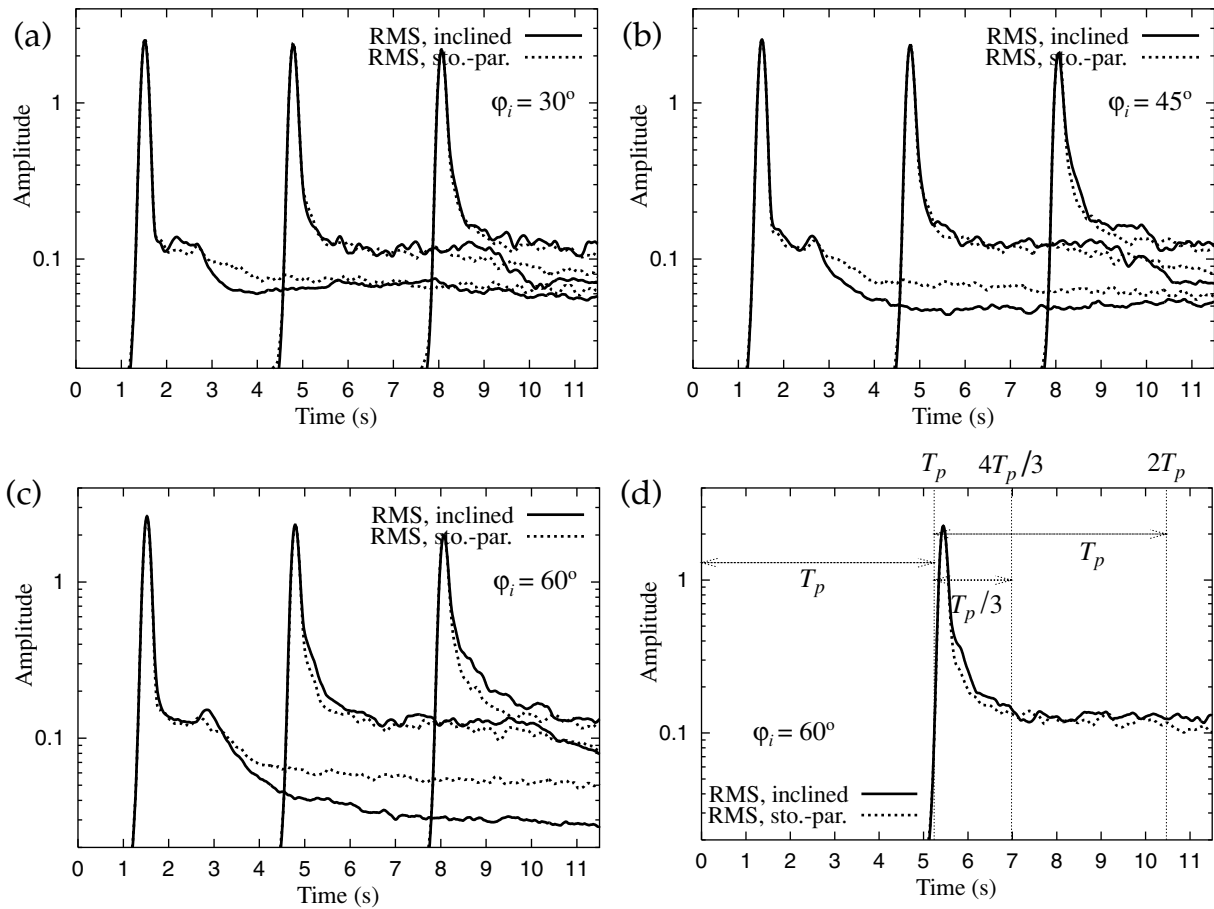


Figure 9. Comparisons of rms envelopes between inclined systems with $a_x = 2005$ m and $a_z = 501$ m and their corresponding paraxial incidence systems at propagation distances of 10.9, 38.1 and 65.4 km. The relative incidence angles (ϕ_i) are (a) 30° , (b) 45° and (c) 60° . Coda level changes with ϕ_i . (d) Empirical division of coda wave trains in terms of stochastic equilibrium. The stochastic equilibrium is established in coda at a time range of $4T_p/3$ to $2T_p$, where T_p is the traveltime of primary waves. For detailed description, we refer to the text.

with propagation distance and the relative incidence angle. The energy accretion is observed for a time of about $T_p/3$ after the primary waves, where T_p is the traveltime of primary wave (see, Fig. 9d). Then the two systems display a similar coda energy level for about $2T_p/3$. The equality in coda level between the two systems, however, is not displayed after a lapse time of about $2T_p$ due to significant energy decrease at coda in oblique system. The coda in paraxial incidence system, on the other hand, displays a consistent level of energy. The discrepancy in coda levels between the two systems appears to increase temporally, and then decreases progressively with time. After a sufficient time, the codas between the two systems display an equivalent level of energy. The time required for the equivalent coda level is proportional to the relative incidence angle.

The observed temporal coda variation can be explained by the energy partition between forward and backward scattered waves. When a wave front is interrupted by heterogeneity, scattered waves are generated. The scattered energy is distributed by the scattering radiation pattern that depends on the shape of heterogeneity and the incidence angle. The scattered waves propagating backward are observed in receivers placed behind the scatterer. On the other hand, forward scattered waves are observed in receivers placed ahead of the scatterer. In particular, the forward scattered waves with a shallow scattering angle propagate just after the primary wave front. Thus, the scattered energy following after the primary wave front

grows continuously with propagation distance (see, the envelopes of $r = 65.39$ km), which results in the energy accretion at early coda. This energy accretion effect is strengthened with the relative incidence angle in oblique incidence system.

The temporal coda level equality between the two systems at a lapse time of $4T_p/3$ to $2T_p$ develops by an energy balance of single-scattered waves. The temporal energy equilibrium does not last after $2T_p$ because the thickness of the layer with anisotropic heterogeneity is limited. In early coda, single scattered waves are dominant. The single scattered waves in coda are the sum of forward and backward single scattered waves. Here, the forward scattered waves are a result of scattering at the heterogeneities in the reverse propagation direction. On the other hand, the backward scattered waves are generated from the heterogeneities in the propagation direction. Thus, when waves are incident into a layer with random heterogeneities, the receivers at short distances record mainly the backward-propagating scattered energy. On the other hand, the receivers placed near the other end of the layer record mainly the forward-propagating scattered energy. The coda envelopes presented in eq. (9) are for receivers at short distances, the sources of forward scattered energy is less than those of backward scattered energy.

When, however, scattered waves are well mixed and multiple scattering is dominant (i.e. the scattered wavefield is diffused), the coda level is the same throughout the receivers in the media. The temporal amplitude variation of seismic coda satisfies a rule (e.g.

Sato & Fehler 1998):

$$A(t) = C \frac{1}{t^p} \exp \left[-\frac{\omega t}{2Q_c} \right], \quad (19)$$

where ω is the angular frequency, t is time, C is a constant, Q_c is the coda quality factor, p is the geometrical spreading parameter with a value 1.0 for 3-D body waves, and 0.5 for 2-D body waves (equivalently, 3-D surface waves). When the coda is diffused, it is dominantly influenced by the intrinsic attenuation (Q_i^{-1}) that counts for the inelastic absorption in the media, that is, $Q_c \approx Q_i$ (Shapiro *et al.* 2000). Thus, the temporal coda variation can be expressed

in terms of the intrinsic absorption and geometrical spreading (Margerin 2005). As the intrinsic attenuation factor is not considered in the modelling (i.e. $Q_i^{-1} = 0$), the temporal amplitude variation of diffused coda can be expressed simply by

$$A(t) = C t^{-p}. \quad (20)$$

As, however, the scattering radiation is dependent on the relative incidence direction and the aspect ratio, the lapse time required for seismic diffusion appears to vary with the geometry. Comparisons between theoretical trend and the envelopes are made for isotropic and anisometric media with $\varphi_i = 0^\circ$ where the diffusion

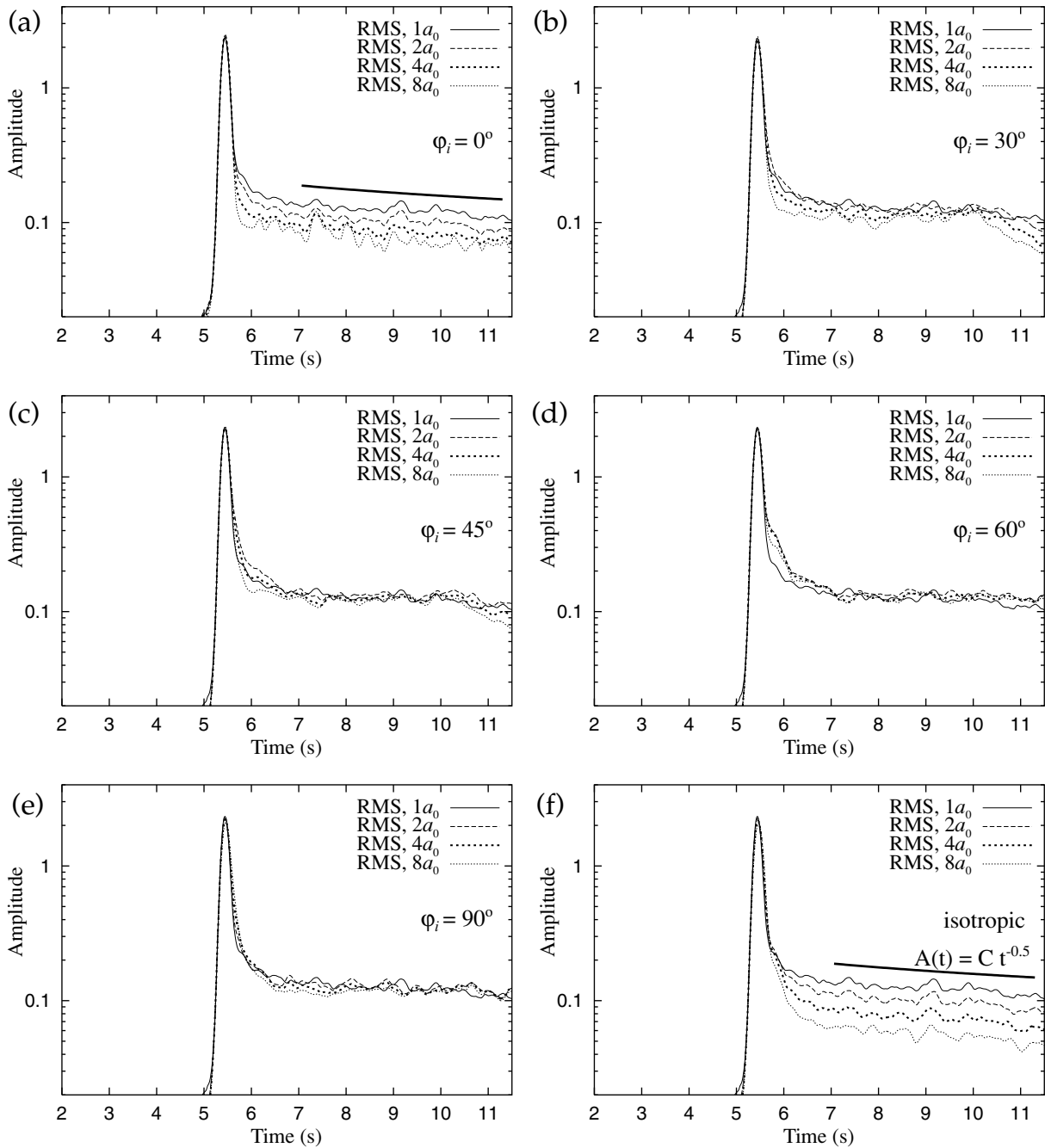


Figure 10. Comparisons of envelopes with changes of a_x ($a_x/a_0 = 1, 2, 4, 8$, and $a_z = a_0 = 501$ m) in anisotropic random media for various relative incidence angles ((a) $\varphi_i = 0^\circ$, (b) 30° , (c) 45° , (d) 60° , (e) 90°) at a propagation distance of 43.6 km. (e) Envelope-level changes with heterogeneity scales ($a_x/a_0 = a_z/a_0 = 1, 2, 4, 8$) in isotropic random media. The coda level change with heterogeneity scale is noticeable in small angles ($\varphi_i = 0^\circ, 30^\circ$), and is weakened with increase of φ_i . The coda level variation with heterogeneity scale much large in isotropic random media.

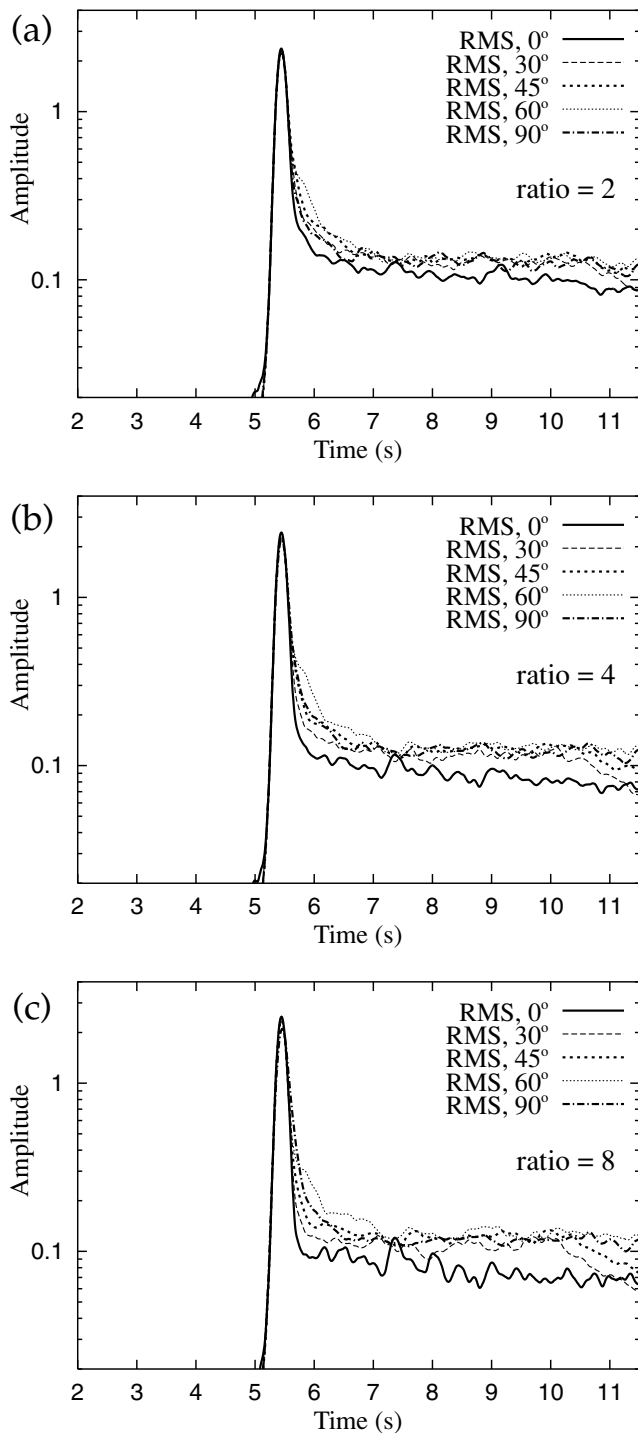


Figure 11. Envelope changes with relative incidence angles ($\varphi_i = 0, 30, 45, 60, 90^\circ$) for three different aspect ratios; (a) $a_x/a_z = 2$, (b) $a_x/a_z = 4$, (c) $a_x/a_z = 8$. The propagation distance is 43.6 km. Energy accretion is made at the early coda wave trains by strengthening of forward scattering with increase of φ_i .

state is established early (Fig. 10). The diffused codas satisfy the trend.

7.2 Implication to field observation

The energy accretion at the early coda of inclined incidence system looks to be an important feature for sounding of heterogeneity

in the Earth's deep interior. In previous studies (e.g. Hedlin *et al.* 1997), precursor amplitude relative to the primary phase (e.g. *PKP*) is used to infer the heterogeneity size and the perturbation strength. The early coda of a rectangular medium is observed partly as in a form of precursor in the spherical Earth. Thus, it appears that systematic under or overestimation of perturbation strength can be made from the precursor analysis without proper consideration of the anisotropic scattered energy distribution by anisometric heterogeneities. Assuming the horizontally elongated heterogeneities in the deep Earth (Kennett *et al.* 1998; Romanowicz 2003), the precursor of deep seismic phase with a large incidence angle will be strengthened by forward scattering.

Fig. 10 shows the coda level variation with aspect ratio ($= a_x/a_z$). The overall coda level variation with aspect ratio agrees with the scattering attenuation variation with aspect ratio in Section 6. The coda level changes significantly with aspect ratio at small φ_i ($0, 30^\circ$), while the change is fairly unnoticeable at large φ_i ($60, 90^\circ$). The coda level change is most significant in isotropic random media (*cf.* Fig. 5).

In Fig. 11 we compare the coda levels of different φ_i ($0, 30, 45, 60, 90^\circ$) for given aspect ratios ($a_h/a_v = 2, 4, 8$). The coda levels of φ_i between 30 and 90° are comparable each other at the time ($4T_p/3 - 2T_p$) of the temporal equality. On the other hand, the coda of $\varphi_i = 0^\circ$ displays a noticeable level change with the aspect ratio. This is because the scattering strength is dependent on the heterogeneity scale in the tangential direction, and the stochastic heterogeneity scale in the tangential direction decreases exponentially with φ_i (see, Fig. 4). We also note that the energy accretion at the early coda is strongest at φ_i of 60° due to the combined effect of diffraction and forward scattering.

From the observation of coda level variation with aspect ratio and the incident angle, we find that the strength of scattering is mostly related with the scale of heterogeneity in the tangential direction. Also, the scale change along the incidence direction rarely affects the scattering strength. As the diffraction and refraction effects are strong in isotropic random media and decrease with the aspect ratio of heterogeneity (Müller & Shapiro 2003), the change of scattering strength with heterogeneity scale is most prominent in isotropic random media. For the estimation of seismic properties of anisometric heterogeneity, the late coda can be analysed. However, the selection of the coda of deep seismic phase at stable stages looks impractical due to the contamination by late-arriving seismic phases. On the other hand, it looks practical to use the data set classified by the incidence angle and infer the physical properties from the assembled observations.

8 DISCUSSION AND CONCLUSIONS

We have investigated the features of scattering in geometrically anisotropic random media. A theoretical expression for scattering attenuation in anisometric elastic random media was formulated. The theoretical scattering attenuation prediction agrees with numerical modelling results well. The scattering in anisometric random media depends mainly on the stochastic scales of heterogeneity in the radial and tangential directions. The tangential scale controls the scattering strength, and the aspect ratio between the radial and tangential scales affects the strength of diffraction and refraction on the heterogeneity.

The coda shape in anisometric random media is highly dependent on the nature of heterogeneity such as aspect ratio and geometry and the wave incidence angle. Coda wave trains can be divided into

several parts following the constituting scattered energy composition. Forward scattering is strengthened with the relative incidence angle, and the forward scattered waves enhance the early coda. The energy accretion by the forward scattered waves increases with the propagation distance and the relative incidence angle. This effect is expected to enhance the precursor and early coda of deep seismic phase travelling through anisometric heterogeneous media.

Scattering level varies sensitively to the tangential scale of heterogeneity. Thus, it appears that the sounding of anisometric heterogeneity in the Earth's deep interior from precursors or coda should be operated by taking account of the incidence direction of the primary phase. To this end it may be a way to examine the coda level variation from seismic data set that is classified by the incidence angle of primary wave. This approach would be particularly useful for deep seismic phases due to their plane wave fronts.

Velocity anisotropy and intrinsic attenuation would be additional factors to be considered for conceivable investigation of heterogeneity in the Earth. However, the strength of velocity anisotropy (e.g. Panning & Romanowicz 2004) is usually trivial compared to the velocity and density perturbation strength. Also, since coda attenuation is the sum of scattering and intrinsic attenuation and the intrinsic attenuation variation is correlated with the scattering attenuation variation, the general scattering feature by anisometric heterogeneity observed in the coda variation is expected to be preserved.

We have considered geometrical anisotropy with an idea that the heterogeneity in the Earth can be represented in terms of continuous stochastic random heterogeneities. However, a localized heterogeneity region composed of discrete anisometric scatterers is also expected in the Earth, for instance partial melting region (Vidale & Hedlin 1998). The investigation of scattering by discrete anisometric heterogeneities may be required in this direction.

ACKNOWLEDGMENTS

TKH is grateful to Prof Brian Kennett for the discussion on deep seismic phases and coda waves and for allowing him to access to the Supercomputer Facility in Australian National University, which is also acknowledged for allocation of computational time. We are grateful to the comments of Prof Rob van der Hilst and two anonymous reviewers, which improved the paper. The research is supported by a grant from DOE/BES at University of California, Santa Cruz.

REFERENCES

Aki, K., 1980. Attenuation of shear waves in the lithosphere for frequencies from 0.05 to 25 Hz, *Phys. Earth planet. Inter.*, **21**, 50–60.
 Aki, K. & Chouet, B., 1975. Origin of coda waves: source, attenuation, and scattering effects, *J. geophys. Res.*, **80**, 3322–3342.
 Aki, K. & Richards, P.G., 1980. *Quantitative Seismology: Theory and Methods*, Vol. 1, W.H. Freeman and Company, San Francisco.
 Birch, F., 1961. The velocity of compressional waves in rocks to 10 kilobars, Part 2, *J. geophys. Res.*, **66**, 2199–2224.
 Burridge, R., 1976. *Some Mathematical Topics in Seismology*, Courant Institute of Mathematical Sciences, New York University, New York.
 Cormier, V.F., 1999. Anisotropy of heterogeneity scale lengths in the lower mantle from PKIKP precursors, *Geophys. J. Int.*, **136**, 373–384.
 Deutsch, C.Y. & Journel, A.G., 1998. *GSLIB: Geostatistical Software Library and User's Guide*, 2nd edn, Oxford University Press, New York.
 Frankel, A., McGarr, A., Bicknell, J., Mori, J., Seeber, L. & Cranswick, E., 1990. Attenuation of high-frequency shear waves in the crust, measurements from New York State, South Africa, and southern California, *J. geophys. Res.*, **95**, 17 441–17 457.

Hedlin, M.A.H., Shearer, P.M. & Earle, P.S., 1997. Seismic evidence for small-scale heterogeneity throughout the Earth's mantle, *Nature*, **387**, 145–150.
 Hong, T.-K., 2004. Scattering attenuation ratios of *P* and *S* waves in elastic media, *Geophys. J. Int.*, **158**, 211–224.
 Hong, T.-K. & Kennett, B.L.N., 2002a. A wavelet-based method for simulation of two-dimensional elastic wave propagation, *Geophys. J. Int.*, **150**, 610–638.
 Hong, T.-K. & Kennett, B.L.N., 2002b. On a wavelet-based method for the numerical simulation of wave propagation, *J. Comput. Phys.*, **183**, 577–622.
 Hong, T.-K. & Kennett, B.L.N., 2003a. Scattering attenuation of 2-D elastic waves: theory and numerical modelling using a wavelet-based method, *Bull. seism. Soc. Am.*, **93**, 922–938.
 Hong, T.-K. & Kennett, B.L.N., 2003b. Modelling of seismic waves in heterogeneous media using a wavelet-based method: application to fault and subduction zones, *Geophys. J. Int.*, **154**, 483–498.
 Hong, T.-K. & Kennett, B.L.N., 2004. Scattering of elastic waves in media with a random distribution of fluid-filled cavities: theory and numerical modelling, *Geophys. J. Int.*, **159**, 961–977.
 Hong, T.-K., Kennett, B.L.N., Wu, R.-S., 2004. Effects of the density perturbation in scattering, *Geophys. Res. Lett.*, **31** (13), L13602, doi:10.1029/2004GL019933.
 Hong, T.-K., Wu, R.-S. & Kennett, B.L.N., 2005. Stochastic features of scattering, *Phys. Earth planet. Inter.*, **148**, 131–148.
 Iooss, B., 1998. Seismic reflection traveltimes in two-dimensional statistically anisotropic random media, *Geophys. J. Int.*, **135**, 999–1010.
 Iooss, B., Blanc-Benon, P. & Lhuillier, C., 2000. Statistical moments of travel times at second order in isotropic and anisotropic random media, *Waves Random Media*, **10**, 381–394.
 Kennett, B.L.N., 1998. On the density distribution within the Earth, *Geophys. J. Int.*, **132**, 374–382.
 Kennett, B.L.N., Engdahl, E.R. & Buland, R., 1995. Constraints on seismic velocities in the earth from travel times, *Geophys. J. Int.*, **122**, 108–124.
 Kennett, B.L.N., Widiyantoro, S. & van der Hilst, R.D., 1998. Joint seismic tomography for bulk sound and shear wave speed in the Earth's mantle, *J. geophys. Res.*, **103**, 12 469–12 493.
 Kravtsov, Y.A., Müller, T.M., Shapiro, S.A. & Buske, S., 2003. Statistical properties of reflection traveltimes in 3-D randomly inhomogeneous and anisometric media, *Geophys. J. Int.*, **154**, 841–851.
 Lee, W.S., Sato, H. & Lee, K., 2003. Estimation of S-wave scattering coefficient in the mantle from envelope characteristics before and after the ScS arrival, *Geophys. Res. Lett.*, **30** (24), 2248, doi:10.1029/2003GL018413.
 Margerin, L., 2005. Introduction to radiative transfer of seismic waves, in *Seismic data analysis with global and local arrays*, eds Levander, A. & Nolet, G., AGU Monograph Series, (in press).
 Margerin, L. & Nolet, G., 2003. Multiple scattering of high-frequency seismic waves in the deep Earth: PKP precursor analysis and inversion for mantle granularity, *J. geophys. Res.*, **108**(B11), 2514, doi:10.1029/2003JB002455.
 Müller, T.M. & Shapiro, S.A., 2003. Amplitude fluctuations due to diffraction and reflection in anisotropic random media: implications for seismic scattering attenuation estimates, *Geophys. J. Int.*, **155**, 139–148.
 Panning, M. & Romanowicz, B., 2004. Inference on flow at the base of Earth's mantle based on seismic anisotropy, *Science*, **303**, 351–353.
 Robertson, G.S. & Woodhouse, J.H., 1996. Ratio of relative *S* to *P* velocity heterogeneity in the lower mantle, *J. geophys. Res.*, **101**(B9), 20 041–20 052.
 Romanowicz, B., 2001. Can we resolve 3D density heterogeneity in the lower mantle?, *Geophys. Res. Lett.*, **28**, 1107–1110.
 Romanowicz, B., 2003. 3D structure of the Earth's lower mantle, *C.R. Geoscience*, **335**, 23–35.
 Roth, M. & Korn, M., 1993. Single scattering theory versus numerical modelling in 2-D random media, *Geophys. J. Int.*, **112**, 124–140.
 Samuelides, Y. & Mukerji, T., 1998. Velocity shift heterogeneous media with anisotropic spatial correlation, *Geophys. J. Int.*, **134**, 778–786.

Sato, H. & Fehler, M., 1998. *Seismic Wave Propagation and Scattering in the Heterogeneous Earth*, Springer-Verlag New York, Inc.

Shapiro, N.M., Campillo, M., Margerin, L., Singh, S.K., Kostoglodov, V. & Pacheco, J., 2000. The energy partitioning and the diffusive character of the seismic coda. *Bull. seism. Soc. Am.*, **90**, 655–665.

Shiomi, K., Sato, H. & Ohtake, M., 1997. Broadband power-bin spectra of well-log data in Japan. *Geophys. J. Int.*, **120**, 57–64.

Vidale, J.E. & Hedlin, M.A.H., 1998. Evidence for partial melt at the core-mantle boundary north of Tonga from the strong scattering of seismic waves. *Nature*, **391**, 682–685.

Vidale, J.E. & Earle, P.S., 2000. Fine-scale heterogeneity in the Earth's inner core. *Nature*, **404**, 273–275.

Wagner, G.S. & Langston, C.A., 1992. A numerical investigation of scattering effects for teleseismic plane wave propagation in a heterogeneous layer over a homogeneous half-space. *Geophys. J. Int.*, **110**, 486–500.

Wu, R.-S. & Aki, K., 1985a. Scattering characteristics of elastic waves by an elastic heterogeneity. *Geophysics*, **50**, 582–595.

Wu, R.-S. & Aki, K., 1985b. Elastic wave scattering by a random medium and the small-scale inhomogeneities in the lithosphere. *J. geophys. Res.*, **90**(B12), 10261–10273.

Yoshimoto, K., Sato, H. & Ohtake, M., 1993. Frequency-dependent attenuation of *P* and *S* waves in the Kanto area, Japan, based on the coda-normalization method. *Geophys. J. Int.*, **114**, 165–174.

APPENDIX A: THEORETICAL DERIVATION OF SCATTERING ATTENUATION EXPRESSION

We derive theoretical scattering attenuation expression for anisometric random media, based on the multiple forward scattering and single backscattering approximation (Hong & Kennett 2003a; Hong 2004). We omit the subscript 0 of symbols for the background properties to simplify mathematical expressions.

Using the scattering forces (f_j^s , $j = x, z$) in (5) and the Green's function (G_{jk} , $j, k = x, z$) for 2-D elastic waves (Burrige 1976, p. 115), we can express scattered wavefield (u_j^s , $j = x, z$ or 1,2) at position \mathbf{x} by the perturbation at \mathbf{x}' as

$$u_j^s(\mathbf{x}) = \sum_{k=1}^2 \int_{\mathbf{S}} f_k^s(\mathbf{x}') G_{jk}(\mathbf{x}, \mathbf{x}') d\mathbf{S}(\mathbf{x}'), \quad (\text{A1})$$

where \mathbf{S} is the area of heterogeneity. The total scattered wavefield is composed of scattered *P* and *S* wavefields (u_r^{PP} , u_t^{PS}), and they can be written by (Hong & Kennett 2003a)

$$\begin{aligned} u_r^{PP}(\mathbf{x}) &= \sin \theta u_x^{PP}(\mathbf{x}) + \cos \theta u_z^{PP}(\mathbf{x}) \\ &= i \sqrt{\frac{k_\alpha}{8\pi|\mathbf{x}|}} C_r(\theta) \exp \left[-i \left(\omega t - k_\alpha |\mathbf{x}| + \frac{\pi}{4} \right) \right] \int_{\mathbf{S}} \xi(\mathbf{x}') \exp[ik_\alpha(z - \mathbf{n} \cdot \mathbf{x}')] d\mathbf{S}(\mathbf{x}'), \\ u_t^{PS}(\mathbf{x}) &= \cos \theta u_x^{PS}(\mathbf{x}) - \sin \theta u_z^{PS}(\mathbf{x}) \\ &= i \sqrt{\frac{k_\alpha^3 \gamma^3}{8\pi|\mathbf{x}|}} C_t(\theta) \exp \left[-i \left(\omega t - k_\beta |\mathbf{x}| + \frac{\pi}{4} \right) \right] \int_{\mathbf{S}} \xi(\mathbf{x}') \exp[ik_\alpha(z - \gamma \mathbf{n} \cdot \mathbf{x}')] d\mathbf{S}(\mathbf{x}'), \end{aligned} \quad (\text{A2})$$

where $C_r(\theta)$ and $C_t(\theta)$ are

$$\begin{aligned} C_r(\theta) &= \sin \theta \left\{ C_1 A_{11}^P(\theta) \sin \theta + 2A_{12}^P(\theta) + C_2 A_{12}^P(\theta) (\cos \theta - 1) \right\} \\ &\quad + \cos \theta \left\{ C_1 A_{21}^P(\theta) \sin \theta + 2A_{22}^P(\theta) + C_2 A_{22}^P(\theta) (\cos \theta - 1) \right\}, \\ C_t(\theta) &= \cos \theta \left\{ C_1 A_{11}^S(\theta) \gamma \sin \theta + 2A_{12}^S(\theta) + C_2 A_{12}^S(\theta) (\gamma \cos \theta - 1) \right\} \\ &\quad - \sin \theta \left\{ C_1 A_{21}^S(\theta) \gamma \sin \theta + 2A_{22}^S(\theta) + C_2 A_{22}^S(\theta) (\gamma \cos \theta - 1) \right\}, \end{aligned} \quad (\text{A3})$$

and A_{ij}^k ($i, j = 1, 2, k = P, S$) is

$$\begin{aligned} A_{11}^P(\theta) &= \sin^2 \theta, \quad A_{12}^P(\theta) = \sin \theta \cos \theta, \quad A_{21}^P(\theta) = -\sin \theta \cos \theta, \quad A_{22}^P(\theta) = \cos^2 \theta, \\ A_{11}^S(\theta) &= \cos^2 \theta, \quad A_{12}^S(\theta) = -\sin \theta \cos \theta, \quad A_{21}^S(\theta) = \sin \theta \cos \theta, \quad A_{22}^S(\theta) = \sin^2 \theta. \end{aligned} \quad (\text{A4})$$

Here, θ is the scattering direction measured from the vertical axis (z , the incidence direction), and \mathbf{n} is the unit vector in \mathbf{x} direction.

In order to estimate the total scattered energy, we calculate ensemble-averaged spectral power density of scattered waves:

$$\begin{aligned} \langle |u_r^{PP}|^2 \rangle &= \frac{k_\alpha^3 W_r}{8\pi|\mathbf{x}|} \\ &\quad \times \int_{\mathbf{S}} \int_{\mathbf{S}'} \langle \xi(\mathbf{x}') \xi(\mathbf{y}') \rangle \exp[ik_\alpha \{ \mathbf{e}_z \cdot (\mathbf{x}' - \mathbf{y}') - \mathbf{n} \cdot (\mathbf{x}' - \mathbf{y}') \}] d\mathbf{S}(\mathbf{x}') d\mathbf{S}(\mathbf{y}'), \\ \langle |u_t^{PS}|^2 \rangle &= \frac{k_\alpha^3 \gamma^3 W_t}{8\pi|\mathbf{x}|} \\ &\quad \times \int_{\mathbf{S}} \int_{\mathbf{S}'} \langle \xi(\mathbf{x}') \xi(\mathbf{y}') \rangle \exp[ik_\alpha \{ \mathbf{e}_z \cdot (\mathbf{x}' - \mathbf{y}') - \gamma \mathbf{n} \cdot (\mathbf{x}' - \mathbf{y}') \}] d\mathbf{S}(\mathbf{x}') d\mathbf{S}(\mathbf{y}'), \end{aligned} \quad (\text{A5})$$

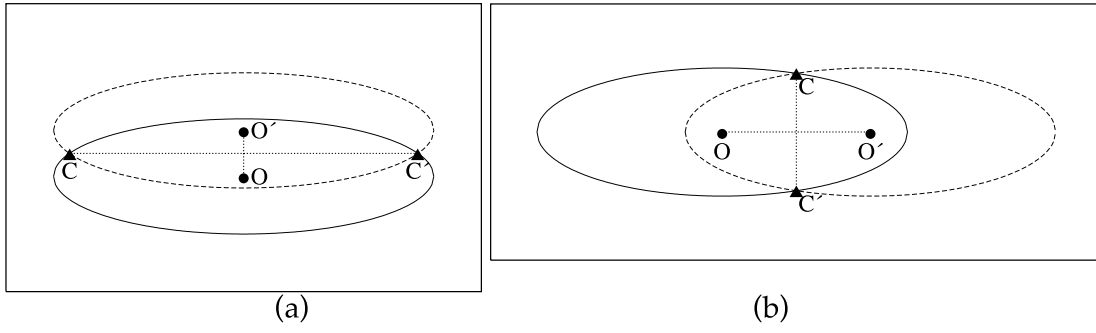


Figure A1. Schematic diagrams of ensemble average (correlation length estimation) of anisometric heterogeneities in (a) vertical and (b) horizontal directions ($O-O'$ direction). The correlation length of anisometric heterogeneities in the direction from O to O' corresponds to the length of overlapping region, and is given by the distance between C and C' (i.e. the distance along the tangential direction). Here, the O and O' correspond to \mathbf{x}' and \mathbf{y}' in eq. (A5). The correlation length in isotropic random media is measured constant in any direction. In practice, the ensemble average of heterogeneity corresponds to 90° -rotated autocorrelation function of the heterogeneity.

where \mathbf{e}_z is the unit vector in z -axis direction, and W_j ($j = r, t$) is

$$W_j = \langle |C_j(\theta)|^2 \rangle = \frac{1}{M} \sum_{i=1}^M |C_j(\theta_i)|^2. \quad (\text{A6})$$

Here, M is a sufficiently large number and θ_i varies randomly between $-\pi$ and π with i . Thus, W_j can be written simply as

$$W_j = \frac{1}{2\pi} \int_{-\pi}^{\pi} [C_j(\phi)]^2 d\phi, \quad (\text{A7})$$

and these are given by

$$\begin{aligned} W_r &= (64 + 7C_1^2 - 64C_2 + 28C_2^2)/32, \\ W_t &= (64 - 64C_2 + 16C_2^2 + \gamma^2 C_1^2 + 4\gamma^2 C_2^2)/32. \end{aligned} \quad (\text{A8})$$

In order to simplify eq. (A5), we make a change of variables from \mathbf{x}' and \mathbf{y}' to \mathbf{p} ($=(\mathbf{x}' + \mathbf{y}')/2$, centre-of-mass coordinate variable) and \mathbf{q} ($=(\mathbf{x}' - \mathbf{y}')$, relative coordinate variable) and express the ensemble of fluctuation ($\langle \xi(\mathbf{x}') \xi(\mathbf{y}') \rangle$) with autocorrelation function ($N(\mathbf{q})$):

$$\begin{aligned} \langle |u_r^{PP}|^2 \rangle &= \frac{k_\alpha^3 W_r \mathbf{S}}{8\pi |\mathbf{x}|} \int_{\mathbf{S}} N^*(\mathbf{q}) \exp[ik_\alpha \mathbf{E}_r \cdot \mathbf{q}] d\mathbf{S}(\mathbf{q}), \\ \langle |u_t^{PS}|^2 \rangle &= \frac{k_\alpha^3 \gamma^3 W_t \mathbf{S}}{8\pi |\mathbf{x}|} \int_{\mathbf{S}} N^*(\mathbf{q}) \exp[ik_\alpha \mathbf{E}_t \cdot \mathbf{q}] d\mathbf{S}(\mathbf{q}), \end{aligned} \quad (\text{A9})$$

where N^* is the orthogonal autocorrelation function (ACF), which corresponds to the 90° -rotated N . As described in Fig. A1, in practice, the ensemble average of anisometric heterogeneity in a given direction ($O - O'$ in the figure) corresponds to the correlation in the tangential direction ($C-C'$). Thus, the measured ACF is observed in a 90° rotated form. The vectors \mathbf{E}_r and \mathbf{E}_t in eq. (A9) are given by

$$\begin{aligned} \mathbf{E}_r &= \mathbf{e}_z - \mathbf{n} = (-\sin\theta, 1 - \cos\theta), \\ \mathbf{E}_t &= \mathbf{e}_z - \gamma \mathbf{n} = (-\gamma \sin\theta, 1 - \gamma \cos\theta). \end{aligned} \quad (\text{A10})$$

The autocorrelation function N and its Fourier transform companion, the power spectral density function \mathcal{P} are given in (13), (15), and (16).

The integrals in (A9) correspond to 2-D Fourier transforms of autocorrelation function, and can be expressed with its normalized power spectral density function (*cf.* Hong & Kennett 2003a)

$$\langle |u_r^{PP}|^2 \rangle = \frac{k_\alpha^3 W_r \mathbf{S}}{(4\pi)^2 |\mathbf{x}|} \mathcal{P}^*(\mathbf{k}_r), \quad \langle |u_t^{PS}|^2 \rangle = \frac{k_\alpha^3 \gamma^3 W_t \mathbf{S}}{(4\pi)^2 |\mathbf{x}|} \mathcal{P}^*(\mathbf{k}_t), \quad (\text{A11})$$

where \mathcal{P}^* is the power spectral density function for N^* , and the wavenumber vector \mathbf{k}_j ($j = r, t$) is given by $k_\alpha \mathbf{E}_j$ from (A10). Here, the power spectral density function satisfies the relationship of $\mathcal{P}^*(\mathbf{k}) = \mathcal{P}(\mathbf{k}^*)$ where $k_i^* = (1 - \delta_{ij})k_j$ ($i, j = x, z$). Thus, (A11) can be rewritten as

$$\langle |u_r^{PP}|^2 \rangle = \frac{k_\alpha^3 W_r \mathbf{S}}{(4\pi)^2 |\mathbf{x}|} \mathcal{P}(\mathbf{k}_r^*), \quad \langle |u_t^{PS}|^2 \rangle = \frac{k_\alpha^3 \gamma^3 W_t \mathbf{S}}{(4\pi)^2 |\mathbf{x}|} \mathcal{P}(\mathbf{k}_t^*). \quad (\text{A12})$$

The energy attenuation corresponds to energy loss per unit area divided by the wavenumber of incident waves, so the resultant scattering attenuation is given by (Hong & Kennett 2003a; Hong 2004)

$$Q_s^{-1} = \frac{\epsilon^2}{k_\alpha \mathbf{S}} \int_\theta \left\{ |u_r^{PP}|^2 + \frac{1}{\gamma} |u_t^{PS}|^2 \right\} dA, \quad (\text{A13})$$

where A is the arc length and dA is given by $r d\theta$ where $r \approx |\mathbf{x}|$ in (A12). The influence of forward scattered waves on scattering attenuation is corrected by introducing minimum scattering angle. Finally, the theoretical scattering attenuation expression is given by

$$\frac{Q_s^{-1}}{\epsilon^2} = \frac{k_\alpha^2 W_r}{(4\pi)^2} \int_{\theta_{\min}}^{2\pi - \theta_{\min}} \mathcal{P}(\mathbf{k}_r^*) d\theta + \frac{k_\alpha^2 \gamma^2 W_t}{(4\pi)^2} \int_{\theta_{\min} + \Delta\phi}^{2\pi - \theta_{\min} - \Delta\phi} \mathcal{P}(\mathbf{k}_t^*) d\theta. \quad (\text{A14})$$